Short Communication

Lorenzo A. Cingolani*, Agnes Thalhammer*, Fanny Jaudon, Jessica Muià and Gabriele Baj

Nanoscale organization of $Ca_V2.1$ splice isoforms at presynaptic terminals: implications for synaptic vesicle release and synaptic facilitation

https://doi.org/10.1515/hsz-2023-0235
Received June 12, 2023; accepted August 1, 2023;
published online September 4, 2023

Abstract: The distance between $Ca_V2.1$ voltage-gated Ca^{2+} channels and the Ca^{2+} sensor responsible for vesicle release at presynaptic terminals is critical for determining synaptic strength. Yet, the molecular mechanisms responsible for a loose coupling configuration of $Ca_V2.1$ in certain synapses or developmental periods and a tight one in others remain unknown. Here, we examine the nanoscale organization of two $Ca_V2.1$ splice isoforms ($Ca_V2.1$[EFa] and $Ca_V2.1$[EFb]) at presynaptic terminals by superresolution structured illumination microscopy. We find that $Ca_V2.1$[EFa] is more tightly co-localized with presynaptic markers than $Ca_V2.1$ [EFb], suggesting that alternative splicing plays a crucial role in the synaptic organization of $Ca_V2.1$ channels.

Keywords: alternative splicing; $Ca_V2.1$; Munc13; presynaptic terminals; structural illumination microscopy; voltage-gated Ca^{2+} channels

***Corresponding authors: Lorenzo A. Cingolani**, Department of Life Sciences, University of Trieste, via Giorgieri 5, I-34127 Trieste, Italy; and Center for Synaptic Neuroscience and Technology (NSYN), Fondazione Istituto Italiano di Tecnologia (IIT), Largo Rosanna Benzi 10, I-16132 Genoa, Italy, E-mail: lcingolani@units.it. https://orcid.org/0000-0001-9538-1659; and **Agnes Thalhammer**, Department of Life Sciences, University of Trieste, via Giorgieri 5, I-34127 Trieste, Italy; and Centro Interdipartimentale di Microscopia Avanzata (CIMA), University of Trieste, via Fleming 31, I-34127 Trieste, Italy, E-mail: agnes.thalhammer@units.it. https://orcid.org/0000-0002-4658-4174

Fanny Jaudon, Department of Life Sciences, University of Trieste, via Giorgieri 5, I-34127 Trieste, Italy; and IRCCS Ospedale Policlinico San Martino, Largo Rosanna Benzi 10, I-16132 Genoa, Italy. https://orcid.org/0000-0001-7648-0977

Jessica Muià, Department of Life Sciences, University of Trieste, via Giorgieri 5, I-34127 Trieste, Italy

Gabriele Baj, Department of Life Sciences, University of Trieste, via Giorgieri 5, I-34127 Trieste, Italy; and Centro Interdipartimentale di Microscopia Avanzata (CIMA), University of Trieste, via Fleming 31, I-34127 Trieste, Italy

The distance between voltage-gated Ca^{2+} channels (VGCCs) and the Ca^{2+} sensors responsible for releasing synaptic vesicles at the active zone of presynaptic terminals plays a crucial role in determining synaptic strength (Dittman and Ryan 2019). Because the diffusion time of Ca^{2+} is proportional to the square of distance, most synapses exhibiting high release probability and reliable transmission in response to single action potentials are characterized by a tight coupling between VGCCs and Ca^{2+} sensors. Conversely, synapses exhibiting low release probability and the ability to facilitate in response to repetitive action potentials generally have a loose coupling between VGCCs and Ca^{2+} sensors (Eggermann et al. 2012). During postnatal development, many glutamatergic excitatory synapses undergo a transition in the configuration of their release machinery. They switch from microdomains, where loosely coupled P/Q- ($Ca_V2.1$) and N-type ($Ca_V2.2$) VGCCs act cooperatively, to nanodomains, where tightly coupled P/Q-type VGCCs efficiently trigger synaptic vesicle exocytosis (Baur et al. 2015; Bornschein et al. 2019; Fedchyshyn and Wang 2005; Kusch et al. 2018; Nakamura et al. 2015).

However, the molecular mechanisms responsible for the transition of $Ca_V2.1$ from a loose to a tight configuration remain unknown. Notably, the pore-forming α_1 subunit of $Ca_V2.1$ (α_{1A}) undergoes extensive alternative splicing, potentially generating thousands of different splice isoforms (Soong et al. 2002). In particular, alternative splicing of two mutually exclusive exons (exons 37a and 37b) produces two isoforms of $Ca_V2.1$ ($Ca_V2.1$[EFa] and $Ca_V2.1$[EFb]), which differ in an EF-hand-like domain located in the proximal C terminus (Figure 1A; Bourinet et al. 1999; Chaudhuri et al. 2004; Jaudon et al. 2020; Soong et al. 2002; Thalhammer et al. 2020).

Here, we use superresolution structured illumination microscopy (SIM) to investigate whether the two isoforms $Ca_V2.1$[EFa] and $Ca_V2.1$[EFb] exhibit distinct nanoscale organization at presynaptic excitatory terminals with varying coupling distances from the active zone. We focused on these isoforms as potential molecular correlates of the

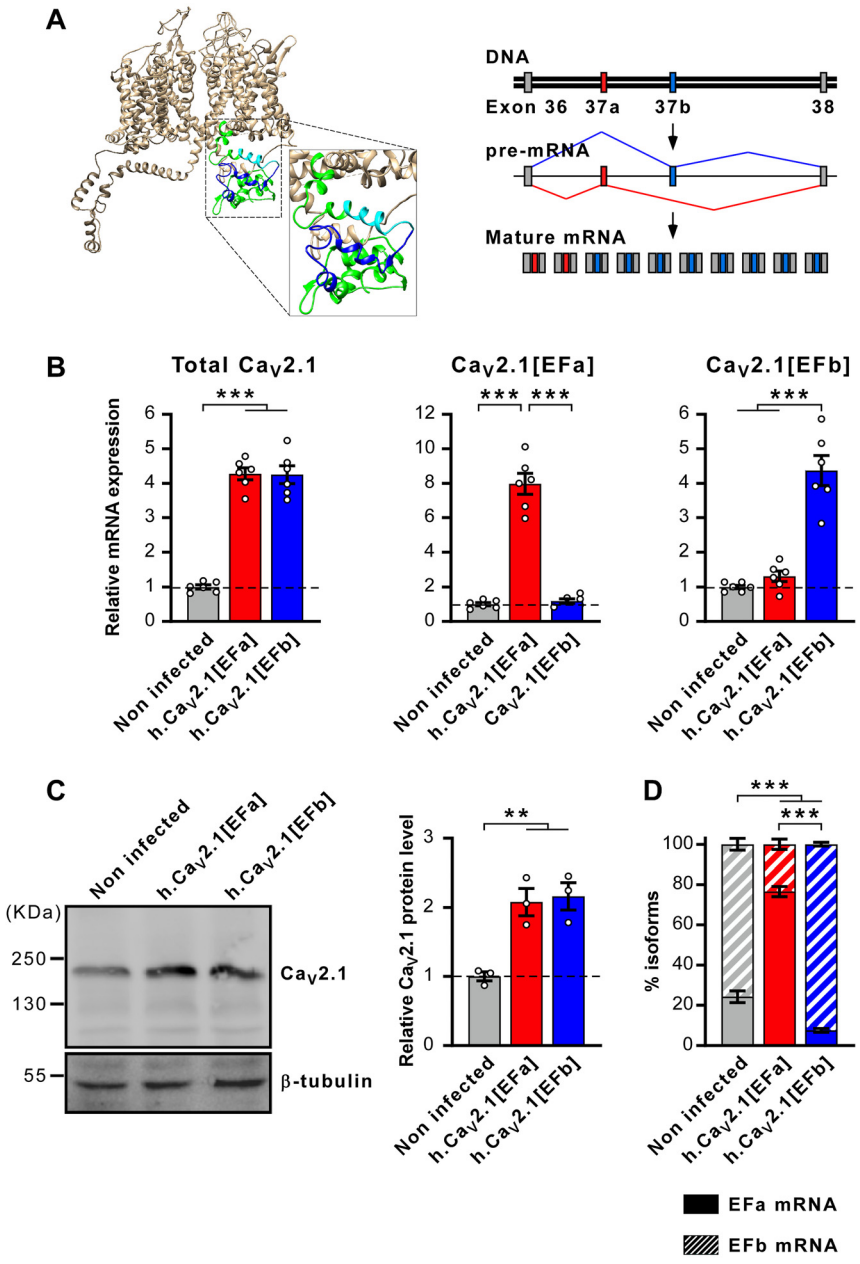

Figure 1: Expression levels of $Ca_V2.1$ splice variants in primary cortical neurons. (A) Left, structural model of human $Ca_V2.1$[EFb] (UniProt ID: O00555; Martinez-Ortiz and Cardozo 2018), highlighting the full C-terminus (in green, cyan and blue colors), the part of the EF-hand-like domain shared between $Ca_V2.1$[EFa] and $Ca_V2.1$[EFb] (the E helix; in cyan) and the 33 residue-long sequence specific to $Ca_V2.1$[EFb] (the loop, the F helix and the downstream residues; in blue). Right, in scale drawing of exons 36, 37a, 37b and 38 of *CACNA1A* ($Ca_V2.1$) and mechanism of mutually exclusive splicing for exons 37a and 37b. Redrawn from (Thalhammer et al. 2020). (B) RT-qPCR quantification of total $Ca_V2.1$, $Ca_V2.1$[EFa] and $Ca_V2.1$[EFa] in 18 DIV primary cortical neurons expressing the indicated constructs (***$p < 0.001$, one-way ANOVA followed by Tukey's post hoc test; $n = 6$ from 2 independent cultures). (C) Left, representative Western blot of membrane-enriched fractions from 18 DIV cortical primary neurons expressing the indicated constructs. Right, quantification of Western blots (**$p < 0.009$, one-way ANOVA followed by Tukey's post hoc test; $n = 3$). (D) The relative abundance of $Ca_V2.1$[EFa] versus $Ca_V2.1$[EFb] splice variants was determined by absolute quantification using calibration curves with known concentrations of recombinant plasmids (***$p < 0.001$, Chi-square test; $n = 6$ from 2 independent cultures). Total $Ca_V2.1$, $Ca_V2.1$[EFa] and $Ca_V2.1$[EFb] in panels B and D were detected with primers m/h.$Ca_V2.1$_Fw/Rv (located in exons 21 and 22), m/h.$Ca_V2.1$[EFa]_Fw and m/h.$Ca_V2.1$[EFa/b]_Rv (located in exons 37a and 38), and m/h.$Ca_V2.1$[EFb]_Fw and m/h.$Ca_V2.1$[EFa/b]_Rv (located in exons 37b and 38), respectively (see Figure S3). For detailed methods, see supplementary materials and Ferrante et al. (2021).

developmental switch in coupling distance between $Ca_V2.1$ and the release machinery for two main reasons. First, the two isoforms have opposite effects on neurotransmitter release and short-term synaptic plasticity. $Ca_V2.1$[EFa] enhances synchronous release and short-term synaptic depression, while $Ca_V2.1$[EFb] promotes asynchronous release and short-term synaptic facilitation (Thalhammer et al. 2017, 2018). Second, while $Ca_V2.1$[EFb] is expressed early in postnatal development, $Ca_V2.1$[EFa] expression increases during the postnatal period, in conjunction with the tightening of the coupling between $Ca_V2.1$ and the neurotransmitter release machinery (Bourinet et al. 1999; Chaudhuri et al. 2004; Soong et al. 2002; Thalhammer et al. 2020; Vigues et al. 2002).

Because of the well-known challenges associated with expressing exogenous $Ca_V2.1$ channels (Heck et al. 2019; Jaudon et al. 2022; Thalhammer et al. 2017), we infected primary cortical neurons at 7 DIV with lentiviruses expressing $Ca_V2.1$[EFa] or $Ca_V2.1$[EFb] under the control of a Synapsin promoter, and performed functional analyses at 18–20 DIV. The use of lentiviruses in conjunction with the Synapsin promoter allowed for a controlled and gradual increase in the levels of $Ca_V2.1$ splice isoforms. Specifically, exogenous expression of either $Ca_V2.1$[EFa] or $Ca_V2.1$[EFb] proved equally effective in augmenting total mRNA levels of $Ca_V2.1$ (approximately 4-fold increase for both $Ca_V2.1$[EFa] or $Ca_V2.1$[EFb]; Figure 1B, left panel) as well as protein levels of $Ca_V2.1$ (approximately 2-fold increase in membrane protein-enriched fractions for both $Ca_V2.1$[EFa] or $Ca_V2.1$[EFb]; Figure 1C). Furthermore, exogenous expression of $Ca_V2.1$[EFa] specifically enhanced the expression of $Ca_V2.1$[EFa], while leaving the levels of $Ca_V2.1$[EFb] unaltered (Figure 1B, middle panel). Conversely, exogenous expression of $Ca_V2.1$[EFb] selectively increased the expression of $Ca_V2.1$[EFb], while keeping the levels of $Ca_V2.1$[EFa] unchanged (Figure 1B, right panel). As a consequence, $Ca_V2.1$[EFa] overexpression led to an inversion in the relative distribution of $Ca_V2.1$[EFa]-$Ca_V2.1$[EFb] from 24–76 %, observed in naïve neurons, to 76–24 %, while $Ca_V2.1$[EFb] overexpression further decreased the relative distribution of $Ca_V2.1$[EFa]-$Ca_V2.1$[EFb] to 7.5–92.5 % (Figure 1D). Exogenous $Ca_V2.1$[EFa] and $Ca_V2.1$[EFb] did not impact total or isoform-specific expression of endogenous $Ca_V2.1$ (Figure S1).

We next assessed whether expression of the two $Ca_V2.1$ splice isoforms changed synaptic levels of $Ca_V2.1$. Consistent with the results from Western blotting analysis (Figure 1C), wide-field fluorescence imaging revealed that both $Ca_V2.1$[EFa] and $Ca_V2.1$[EFb] significantly increased $Ca_V2.1$ fluorescence intensity to a similar degree without altering expression of bassoon and vGlut1 (Figure S2A, B). However, when we employed SIM to obtain super-resolved fluorescence images, it became apparent that neither $Ca_V2.1$[EFa] nor $Ca_V2.1$[EFb] had any discernable impact on the number or size of $Ca_V2.1$ puncta (Figure 2A–C and S2C). Likewise, no changes were observed in the number or size of presynaptic boutons (identified by co-labeling for bassoon) or excitatory presynaptic boutons (identified by co-labeling for vGlut1; Figure 2A–C and S2C). Taken together, these results suggest that the exogenous $Ca_V2.1$ isoforms are expressed synaptically without causing major structural alterations to synaptic boutons.

In line with previous findings (Thalhammer et al. 2017), the expression of $Ca_V2.1$[EFa] resulted in an increased level of colocalization between $Ca_V2.1$ and the presynaptic cytomatrix protein bassoon. Under naïve condition, only 12 % of the area of bassoon positive puncta co-localized with $Ca_V2.1$; this percentage rose to 19 % in the presence of $Ca_V2.1$[EFa], while it remained unchanged at 13 % with $Ca_V2.1$[EFb] (Figure 2D, E and S2D, left). Interestingly, more pronounced effects were observed for excitatory synapses. Expression of $Ca_V2.1$[EFa] resulted in an increase in the level of colocalization between $Ca_V2.1$ and vGlut1 from 20 to 26 %, whereas $Ca_V2.1$[EFb] reduced it to 14 % (Figure 2F, G and S2D, right). These results collectively suggest that $Ca_V2.1$[EFa] is more tightly co-localized with presynaptic excitatory boutons than its mutually exclusive isoform $Ca_V2.1$[EFb].

Recent reports have highlighted the crucial role of Munc13-1 proteins in the vesicle release machinery. The number of Munc13-1 clusters at the active zone correlates closely with the number of docked vesicles and the estimated number of release complexes (Rebola et al. 2019; Sakamoto et al. 2018). In light of these findings, we co-stained for $Ca_V2.1$ and Munc13-1 to assess the nanoscale arrangement of presynaptic $Ca_V2.1$ in relation to Munc13-1.

Similar to what we observed for Bassoon and vGlut1, neither $Ca_V2.1$[EFa] nor $Ca_V2.1$[EFb] had any noticeable effect on fluorescence intensity or number and size of Munc13-1 puncta (Figure 3A, B). However, similar to the findings with Bassoon, expression of $Ca_V2.1$[EFa] led to an enhanced level of co-localization between $Ca_V2.1$ and Munc13-1. Under naïve condition, only 12 % of the area of Munc13-1 positive puncta co-localized with $Ca_V2.1$; this percentage increased to 19 % in the presence of $Ca_V2.1$[EFa], while it remained unchanged at 13 % with $Ca_V2.1$[EFb] (Figure 3C, D). To estimate the minimum distance between $Ca_V2.1$ and Munc13-1 at the active zone in the three experimental conditions, Gaussian bell curves were fit to the fluorescence intensity profiles of partially overlapping $Ca_V2.1$ and Munc13-1 puncta along the lines connecting their centers of mass (Figure 3E, F). Interestingly, the distance measured 32 nm for naïve neurons and the $Ca_V2.1$[EFa] condition, but increased to 64 nm in the $Ca_V2.1$[EFb] condition (Figure 3F, G).

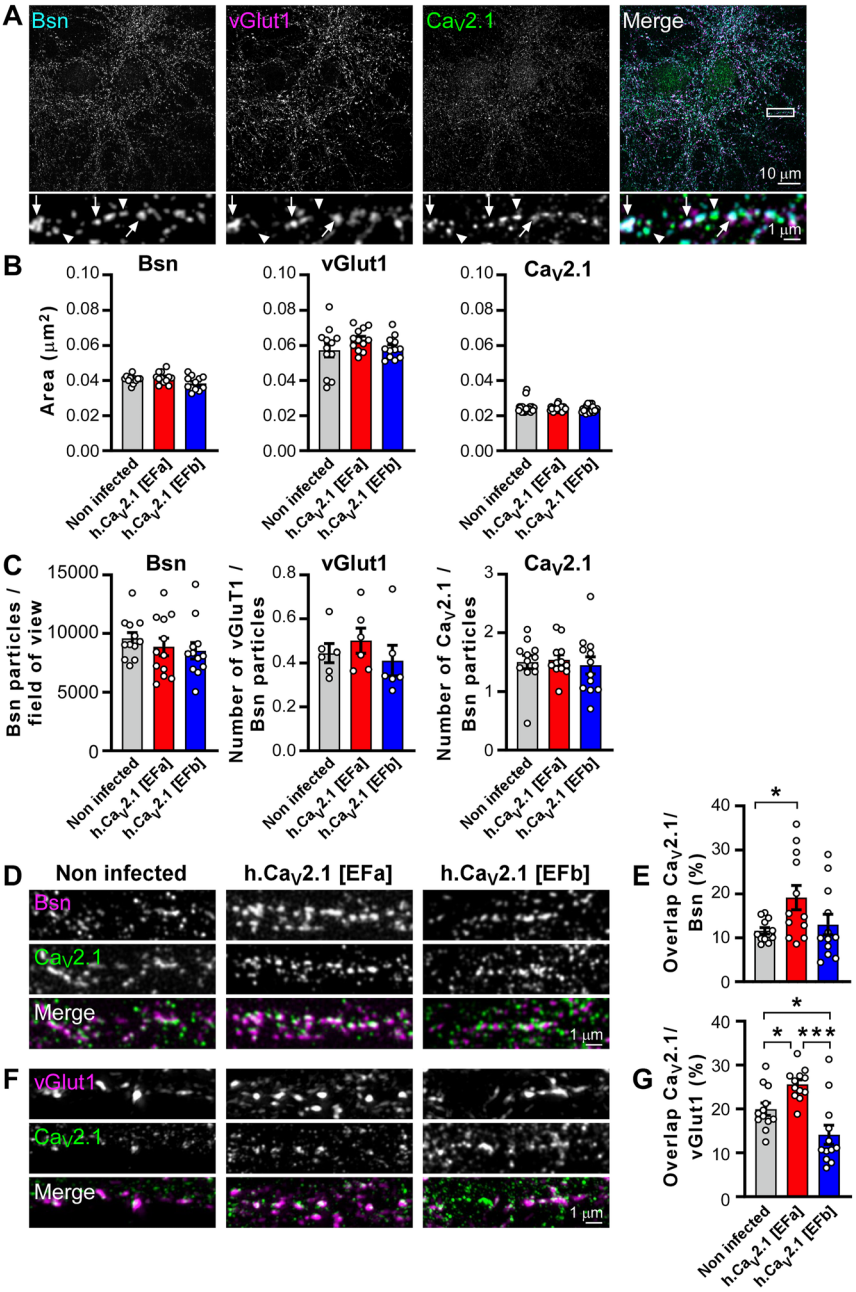

Figure 2: $Ca_V2.1$[EFa] is more efficiently targeted to excitatory synaptic boutons than $Ca_V2.1$[EFb]. (A) Reconstructed and Z-projected SIM images of primary cortical neurons for Bassoon (Bsn), vGlut1 and $Ca_V2.1$. Top, full field of view; bottom, magnification of indicated ROI. Arrowheads indicate $Ca_V2.1$ puncta co-localizing with Bsn; arrows indicate $Ca_V2.1$ puncta co-localizing with both Bsn and vGlut1. (B) Area of Bsn, vGlut1 and $Ca_V2.1$ puncta for the indicated experimental conditions. The size of Bsn, vGlut1 and $Ca_V2.1$ puncta is not altered by exogenous expression of either $Ca_V2.1$[EFa] or $Ca_V2.1$[EFb] ($p = 0.610$, $p = 0.353$ and $p = 0.456$, and $n = 12$, 12 and 24 fields of views for Bsn, vGlut1 and $Ca_V2.1$, respectively; one-way ANOVA). (C) Left, total number of Bsn particles per field of view; middle, number of vGlut1 particles normalized to the number of Bsn particles; right, number of $Ca_V2.1$ particles normalized to the number of Bsn particles. The number of Bsn, vGlut1 and $Ca_V2.1$ particles is not altered by exogenous expression of either $Ca_V2.1$[EFa] or $Ca_V2.1$[EFb] ($p = 0.522$, $p = 0.542$ and $p = 0.851$, and $n = 12$, 6 and 12 fields of views for Bsn, vGlut1 and $Ca_V2.1$, respectively; one-way ANOVA). (D) Reconstructed and Z-projected SIM images of Bsn and $Ca_V2.1$. White in merge highlights colocalization. (E) Percentage of Bsn puncta area co-localized with $Ca_V2.1$ puncta for images as in (D). Expression of $Ca_V2.1$[EFa] increases colocalization of $Ca_V2.1$ with Bsn (*$p = 0.018$, one-way ANOVA followed by Tukey's *post hoc* test, $n = 12$ fields of views per condition). (F) As in (D) but for vGlut1 and $Ca_V2.1$. (G) Percentage of vGlut1 puncta area co-localized with $Ca_V2.1$ puncta for images as in (F). Expression of $Ca_V2.1$[EFa] increases colocalization of $Ca_V2.1$ with vGlut1 while expression of $Ca_V2.1$[EFb] decreases it (*$p < 0.05$, ***$p < 0.001$, one-way ANOVA followed by Tukey's *post hoc* test, $n = 12$ fields of views per condition).

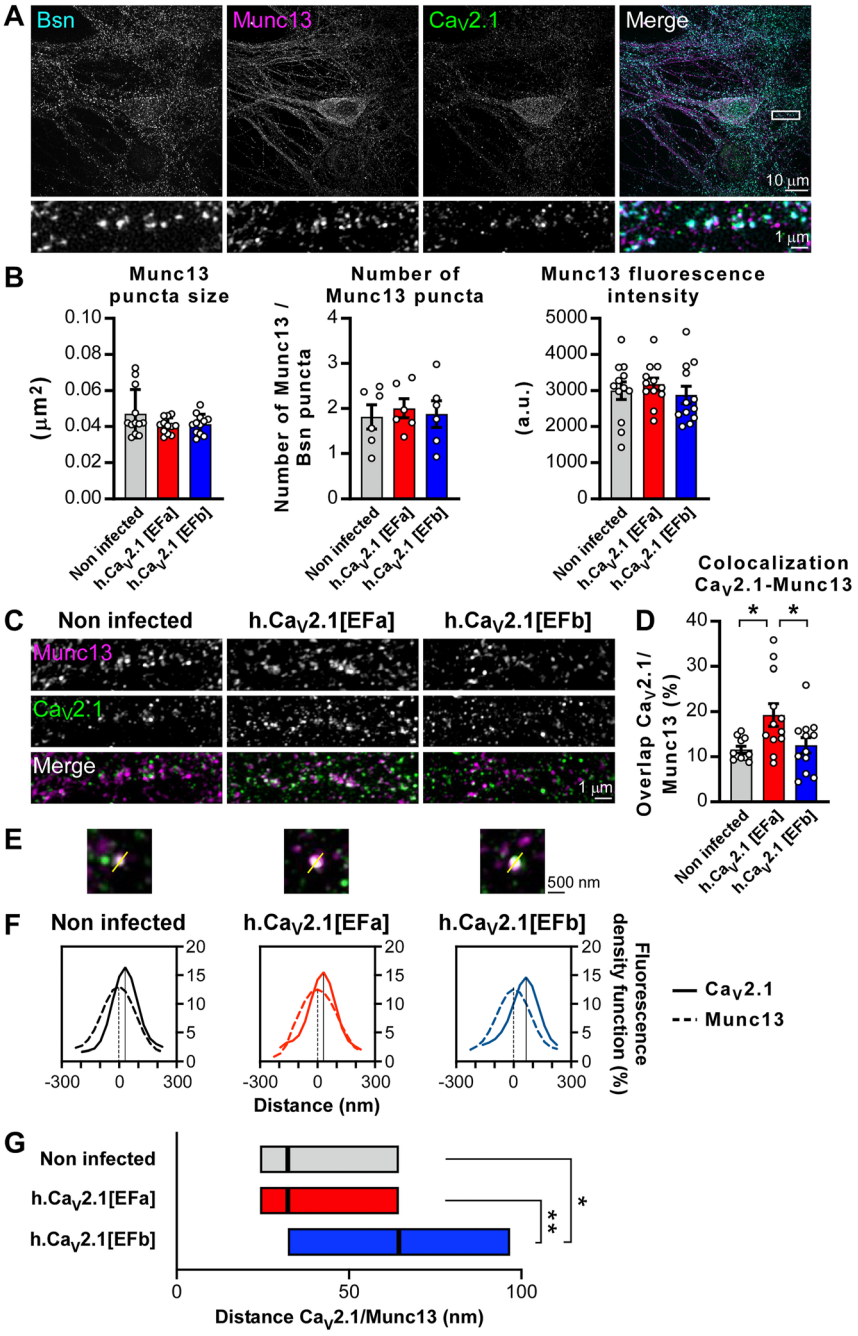

Figure 3: $Ca_V2.1$[EFa] is more tightly co-localized with the active zone protein Munc13-1 than $Ca_V2.1$[EFb]. (A) Reconstructed and Z-projected SIM images of primary cortical neurons for Bsn, Munc13-1 and $Ca_V2.1$. Top, full field of view; bottom, magnification of indicated ROI. (B) Left, area of Munc13-1 puncta for the indicated experimental conditions ($p = 0.141$, $n = 12$ fields of view per condition, one-way ANOVA). Middle, number of Munc13-1 particles normalized to the number of Bsn particles. ($p = 0.872$, one-way ANOVA, $n = 6$ fields of view per condition). Right, quantification of Munc13-1 fluorescence intensity from wide-field fluorescence images before SIM reconstruction ($p = 0.63$, one-way ANOVA, $n = 12$ fields of view). Size and number of puncta as well as fluorescence intensity of Munc13-1 are not altered by exogenous expression of either $Ca_V2.1$[EFa] or $Ca_V2.1$[EFb]. (C) Reconstructed and Z-projected SIM images of Munc13-1 and $Ca_V2.1$. White in merge highlights colocalization. (D) Percentage of Munc13-1 puncta area co-localized with $Ca_V2.1$ puncta for images as in (C). Expression of $Ca_V2.1$[EFa] increases colocalization of $Ca_V2.1$ with Munc13-1 (*$p < 0.04$, one-way ANOVA followed by Tukey's post hoc test, $n = 12$ fields of view). (E) Munc13-1 puncta (magenta) co-localized with $Ca_V2.1$ (green) for the indicated experimental conditions. Scanning line used for the intensity fluorescence profile is indicated in yellow. (F) Intensity fluorescence profile for images as in (E; $n = 26$ boutons). (G) Box plot of the distance between the peaks of the fluorescence intensity profiles for Munc13-1 and $Ca_V2.1$ puncta as for panels (E) and (F). Thick lines indicate median, boxes extend from the 25th to 75th percentiles. Expression of $Ca_V2.1$[EFa] increases the distance between Munc13-1 and $Ca_V2.1$ (*$p = 0.012$ and **$p = 0.008$, one-way Brown-Forsythe ANOVA followed by Dunnett T3 *post hoc* test, $n = 26$ boutons).

Collectively, these findings indicate significant and relevant differences in the spatial organization of two mutually exclusive isoforms of $Ca_V2.1$ at the active zone. $Ca_V2.1$[EFa] is positioned in close proximity to Munc13-1, indicative of its role in supporting synchronous release of synaptic vesicle through the generation of large (>10 μM) and brief (<1 ms) nanodomain calcium signals that activate fast low-affinity calcium sensors, such as synaptotagmin 1 (Eggermann et al. 2012; Geppert et al. 1994; Thalhammer et al. 2017). On the other hand, $Ca_V2.1$[EFb] is only loosely coupled to Munc13-1, indicative of its involvement in boosting the residual calcium signal (<1 μM) that persists for tens to hundreds of milliseconds in presynaptic boutons, thus contributing to short-term synaptic facilitation and asynchronous release, possibly via slow high-affinity calcium sensors, such as synaptotagmin 7 (Jackman et al. 2016; Kaeser and Regehr 2014; Thalhammer et al. 2017). Considering the limitations in spatial resolutions of the SIM technique, our estimations of the physical distance between Munc13-1 and the two $Ca_V2.1$ isoforms align well with electron microscopy studies that reported distances of 20 and 50 nm between Munc13-1 and $Ca_V2.1$ at strong and weak synapses, respectively (Rebola et al. 2019). We propose therefore that alternative splicing of $Ca_V2.1$ at exons 37a/b may account for many of the temporal and spatial variations in the nanoscale organization of $Ca_V2.1$ at the active zone that have recently been reported (Baur et al. 2015; Cingolani et al. 2019; Holderith et al. 2012; Kusch et al. 2018; Nakamura et al. 2015; Rebola et al. 2019).

Acknowledgments: This work was supported by the Telethon foundation (proposal ID: GGP19181 to LAC).

Research ethics: All animal procedures were in accordance with the guidelines for animal welfare used in scientific research of the Italian Government and the local governance.

Author contributions: AT and LAC concieved the project. AT, FJ, GB and LAC designed experiments. AT, FJ and JM performed experiments, AT and FJ analysed data, AT, FJ and LAC prepared figures and wrote the paper. The authors have accepted responsibility for the entire content of this manuscript and approved its submission.

Competing interests: The authors state no conflict of interest.

Research funding: Telethon foundation, proposal GGP19181.

Data availability: The raw data can be obtained on request from the corresponding author.

References

Baur, D., Bornschein, G., Althof, D., Watanabe, M., Kulik, A., Eilers, J., and Schmidt, H. (2015). Developmental tightening of cerebellar cortical synaptic influx-release coupling. J. Neurosci. 35: 1858–1871.

Bornschein, G., Eilers, J., and Schmidt, H. (2019). Neocortical high probability release sites are formed by distinct Ca^{2+} channel-to-release sensor topographies during development. Cell Rep 28: 1410–1418 e1414.

Bourinet, E., Soong, T.W., Sutton, K., Slaymaker, S., Mathews, E., Monteil, A., Zamponi, G.W., Nargeot, J., and Snutch, T.P. (1999). Splicing of α1A subunit gene generates phenotypic variants of P- and Q-type calcium channels. Nat. Neurosci. 2: 407–415.

Chaudhuri, D., Chang, S.Y., DeMaria, C.D., Alvania, R.S., Soong, T.W., and Yue, D.T. (2004). Alternative splicing as a molecular switch for Ca^{2+}/calmodulin-dependent facilitation of P/Q-type Ca^{2+} channels. J. Neurosci. 24: 6334–6342.

Cingolani, L.A., Vitale, C., and Dityatev, A. (2019). Intra- and extracellular pillars of a unifying framework for homeostatic plasticity: a crosstalk between metabotropic receptors and extracellular matrix. Front Cell Neurosci 13: 513.

Dittman, J.S. and Ryan, T.A. (2019). The control of release probability at nerve terminals. Nat. Rev. Neurosci. 20: 177–186.

Eggermann, E., Bucurenciu, I., Goswami, S.P., and Jonas, P. (2012). Nanodomain coupling between Ca^{2+} channels and sensors of exocytosis at fast mammalian synapses. Nat. Rev. Neurosci. 13: 7–21.

Fedchyshyn, M.J. and Wang, L.Y. (2005). Developmental transformation of the release modality at the calyx of Held synapse. J. Neurosci. 25: 4131–4140.

Ferrante, D., Sterlini, B., Prestigio, C., Marte, A., Corradi, A., Onofri, F., Tortarolo, G., Vicidomini, G., Petretto, A., Muia, J., et al. (2021). PRRT2 modulates presynaptic Ca^{2+} influx by interacting with P/Q-type channels. Cell Rep 35: 109248.

Geppert, M., Goda, Y., Hammer, R.E., Li, C., Rosahl, T.W., Stevens, C.F., and Sudhof, T.C. (1994). Synaptotagmin I: a major Ca^{2+} sensor for transmitter release at a central synapse. Cell 79: 717–727.

Heck, J., Parutto, P., Ciuraszkiewicz, A., Bikbaev, A., Freund, R., Mitlohner, J., Andres-Alonso, M., Fejtova, A., Holcman, D., and Heine, M. (2019). Transient confinement of Ca(V)2.1 Ca^{2+}-channel splice variants shapes synaptic short-term plasticity. Neuron 103: 66–79 e12.

Holderith, N., Lorincz, A., Katona, G., Rozsa, B., Kulik, A., Watanabe, M., and Nusser, Z. (2012). Release probability of hippocampal glutamatergic terminals scales with the size of the active zone. Nat. Neurosci. 15: 988–997.

Jackman, S.L., Turecek, J., Belinsky, J.E., and Regehr, W.G. (2016). The calcium sensor synaptotagmin 7 is required for synaptic facilitation. Nature 529: 88–91.

Jaudon, F., Baldassari, S., Musante, I., Thalhammer, A., Zara, F., and Cingolani, L.A. (2020). Targeting alternative splicing as a potential therapy for episodic ataxia type 2. Biomedicines 8, https://doi.org/10.3390/biomedicines8090332.

Jaudon, F., Thalhammer, A., Zentilin, L., and Cingolani, L.A. (2022). CRISPR-mediated activation of autism gene Itgb3 restores cortical network excitability via mGluR5 signaling. Mol Ther Nucleic Acids 29: 462–480.

Kaeser, P.S. and Regehr, W.G. (2014). Molecular mechanisms for synchronous, asynchronous, and spontaneous neurotransmitter release. Annu. Rev. Physiol. 76: 333–363.

Kusch, V., Bornschein, G., Loreth, D., Bank, J., Jordan, J., Baur, D., Watanabe, M., Kulik, A., Heckmann, M., Eilers, J., et al. (2018). Munc13-3 is required for the developmental localization of Ca^{2+} channels to active zones and the nanopositioning of Ca(v)2.1 near release sensors. Cell Rep 22: 1965–1973.

Martinez-Ortiz, W. and Cardozo, T.J. (2018). An improved method for modeling voltage-gated ion channels at atomic accuracy applied to human Cav channels. Cell Rep 23: 1399–1408.

Nakamura, Y., Harada, H., Kamasawa, N., Matsui, K., Rothman, J.S., Shigemoto, R., Silver, R.A., DiGregorio, D.A., and Takahashi, T. (2015). Nanoscale distribution of presynaptic Ca^{2+} channels and its impact on vesicular release during development. Neuron 85: 145–158.

Rebola, N., Reva, M., Kirizs, T., Szoboszlay, M., Lorincz, A., Moneron, G., Nusser, Z., and DiGregorio, D.A. (2019). Distinct nanoscale calcium channel and synaptic vesicle topographies contribute to the diversity of synaptic function. Neuron 104: 693–710 e699.

Sakamoto, H., Ariyoshi, T., Kimpara, N., Sugao, K., Taiko, I., Takikawa, K., Asanuma, D., Namiki, S., and Hirose, K. (2018). Synaptic weight set by Munc13-1 supramolecular assemblies. Nat. Neurosci. 21: 41–49.

Soong, T.W., DeMaria, C.D., Alvania, R.S., Zweifel, L.S., Liang, M.C., Mittman, S., Agnew, W.S., and Yue, D.T. (2002). Systematic identification of splice variants in human P/Q-type channel α1(2.1) subunits: implications for current density and Ca^{2+}-dependent inactivation. J. Neurosci. 22: 10142–10152.

Thalhammer, A., Contestabile, A., Ermolyuk, Y.S., Ng, T., Volynski, K.E., Soong, T.W., Goda, Y., and Cingolani, L.A. (2017). Alternative splicing of P/Q-Type Ca^{2+} channels shapes presynaptic plasticity. Cell Rep 20: 333–343.

Thalhammer, A., Jaudon, F., and Cingolani, L.A. (2018). Combining optogenetics with artificial microRNAs to characterize the effects of gene knockdown on presynaptic function within intact neuronal circuits. J Vis Exp 133: 1–8.

Thalhammer, A., Jaudon, F., and Cingolani, L.A. (2020). Emerging roles of activity-dependent alternative splicing in homeostatic plasticity. Front Cell Neurosci 14: 104.

Vigues, S., Gastaldi, M., Massacrier, A., Cau, P., and Valmier, J. (2002). The α1A subunits of rat brain calcium channels are developmentally regulated by alternative RNA splicing. Neuroscience 113: 509–517.

Supplementary Material: This article contains supplementary material (https://doi.org/10.1515/hsz-2023-0235).

Supplemental Material

Nanoscale organization of $Ca_V2.1$ splice isoforms at presynaptic terminals: Implications for synaptic vesicle release and synaptic facilitation

Agnes Thalhammer[1, 2,*], Fanny Jaudon[1, 3], Jessica Muià[1], Gabriele Baj[1, 2] and Lorenzo A. Cingolani[1, 4, *]

[1] Department of Life Sciences, University of Trieste, 34127 Trieste, Italy

[2] Centro Interdipartimentale di Microscopia Avanzata (CIMA), University of Trieste, 34127 Trieste, Italy

[3] IRCCS Ospedale Policlinico San Martino, 16132 Genoa, Italy

[4] Center for Synaptic Neuroscience and Technology (NSYN), Fondazione Istituto Italiano di Tecnologia (IIT), 16132 Genoa, Italy

Content:

Supplemental Figures

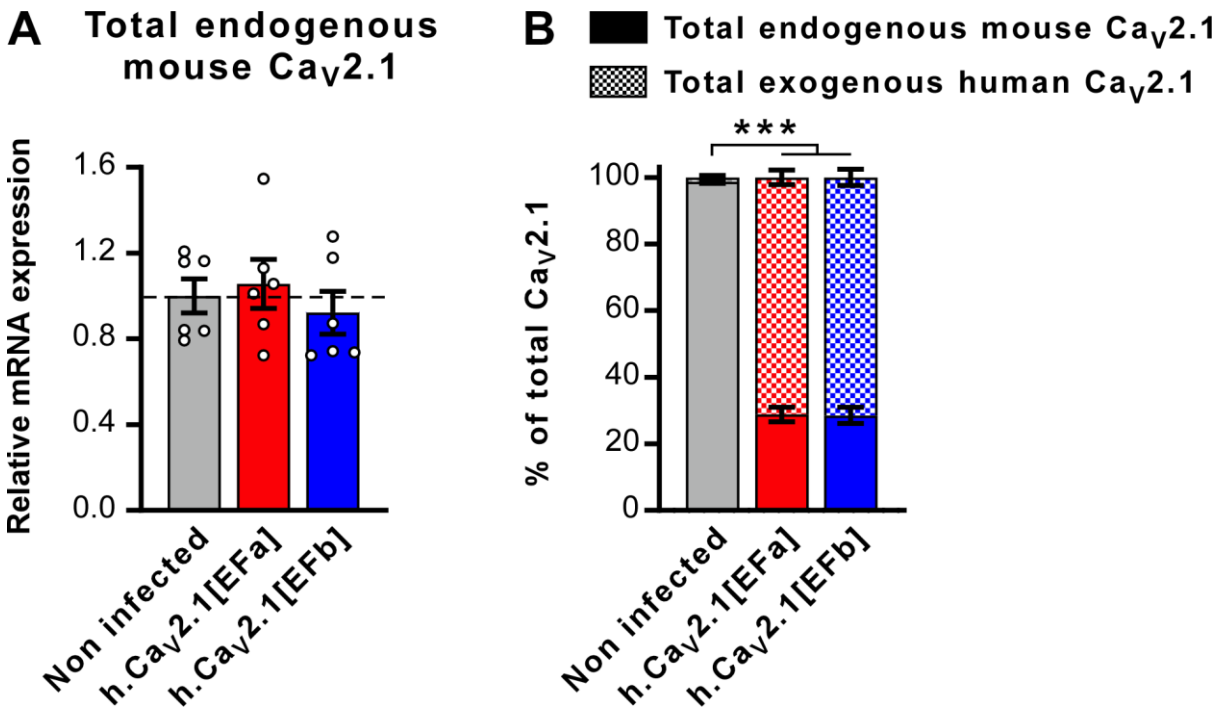

Figure S1. Levels of endogenous mouse $Ca_V2.1$ are not affected by exogenous expression of human $Ca_V2.1$. (A) RT-qPCR quantification of endogenous mouse $Ca_V2.1$ in 18 DIV primary cortical neurons expressing the indicated constructs ($p > 0.05$, one-way ANOVA; n = 6 from 2 independent cultures). **(B)** The relative abundance of endogenous mouse versus exogenous human $Ca_V2.1$ was determined by absolute quantification using calibration curves with known concentrations of recombinant plasmids (***$p<0.001$, Chi-square test; n = 6 from 2 independent cultures). Total endogenous mouse $Ca_V2.1$ and total exogenous human $Ca_V2.1$ in panels A and B were detected with primers m.$Ca_V2.1$_Fw/Rv (located in exons 2 and 3) and h.$Ca_V2.1$_Fw/Rv (located in the N-terminal AU1 tag and exon 1), respectively (see **Fig S3**).

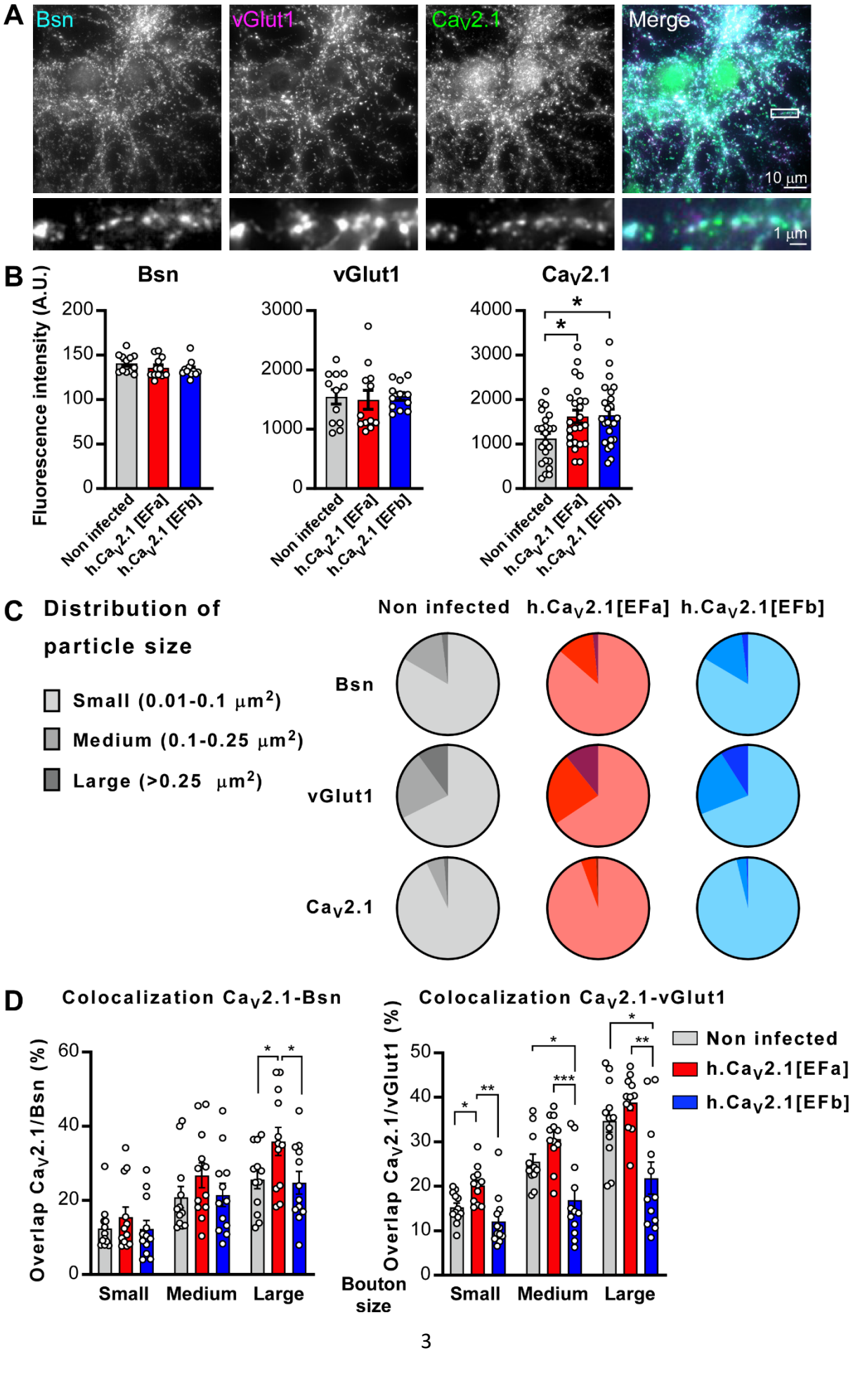
A
Bsn
vGlut1
CaV2.1
Merge
10 µm
1 µm
B
Bsn
vGlut1
CaV2.1
Fluorescence intensity (A.U.)
200
150
100
50
0
3000
2000
1000
0
4000
3000
2000
1000
0
*
*
Non infected
h.CaV2.1 [EFa]
h.CaV2.1 [EFb]
C
Distribution of particle size
Small (0.01-0.1 µm2)
Medium (0.1-0.25 µm2)
Large (>0.25 µm2)
Non infected
h.CaV2.1[EFa]
h.CaV2.1[EFb]
Bsn
vGlut1
CaV2.1
D
Colocalization CaV2.1-Bsn
Overlap CaV2.1/Bsn (%)
60
40
20
0
* *
Small
Medium
Large
Colocalization CaV2.1-vGlut1
Overlap CaV2.1/vGlut1 (%)
50
40
30
20
10
0
* **
* ***
* **
Bouton size
Small
Medium
Large
Non infected
h.CaV2.1[EFa]
h.CaV2.1[EFb]

Figure S2. Further analysis of fluorescence intensity and colocalization for $Ca_V2.1$, Bsn and vGlut1. (A) Wide-field fluorescence images of the same primary cortical neurons shown in Fig 2A before SIM reconstruction. **(B)** Quantification of image fluorescence intensity for Bassoon (Bsn), vGlut1 and $Ca_V2.1$ for images as in (A). Fluorescence intensity of $Ca_V2.1$ increases to the same extent upon expression of either $Ca_V2.1$[EFa] or $Ca_V2.1$[EFb] (*p<0.05, one-way ANOVA followed by Tukey's post hoc test; n = 12, 12 and 24 fields of view for Bsn, vGlut1 and $Ca_V2.1$, respectively). **(C)** Proportions of small (0.01 - 0.1 μm^2), medium (0.1 - 0.25 μm^2) and large (> 0.25 μm^2) Bsn, vGlut1 and $Ca_V2.1$ puncta for the three indicated experimental conditions. The relative proportions of puncta size are not affected by exogenous expression of either $Ca_V2.1$[EFa] or $Ca_V2.1$[EFb] ($p > 0.05$, Chi-square test; n = 12, 12 and 24 fields of view for Bsn, vGlut1 and $Ca_V2.1$, respectively). **(D)** Left, analysis of colocalization between $Ca_V2.1$ and Bsn as for Fig 2D, E but done separately for boutons of different size, as indicated. Right, analysis of colocalization between $Ca_V2.1$ and vGlut1 as for Fig 2F, G but done separately for boutons of different size, as indicated (*p<0.05, **p<0.01, ***p<0.001, 2-way ANOVA followed by Tukey's post hoc test; n = 12 fields of views per condition).

A

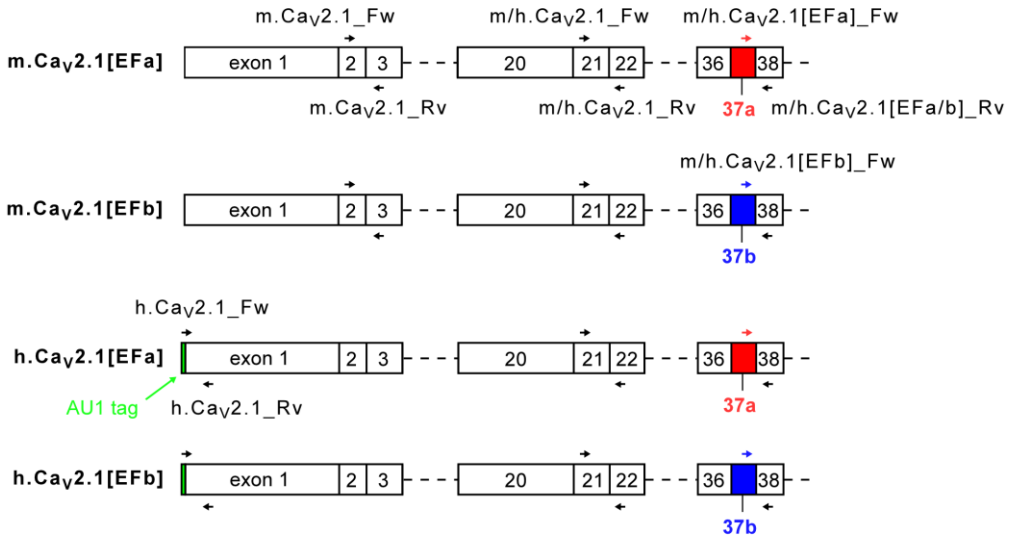

B

Target	Fw primer name	Forward primer sequence (5' → 3')	Rv primer name	Reverse primer sequence (5' → 3')
mouse $Ca_V2.1$	m.Ca_V2.1_Fw	CCTGATGATGACAAGACACC	m.CaV2.1_Rv	TTCCAGCCTCAAAACAGAAG
$Ca_V2.1$ (mouse + human)	m/h.Ca_V2.1_Fw	AACAAAAACGCCAACCCAGA	m/h.Ca_V2.1_Rv	AAGTAGCGCAGGTTCAGGAT
human $Ca_V2.1$	h.Ca_V2.1_Fw	CCTACAGATACATCGGAGGAGC	h.Ca_V2.1_Rv	GGGGATGGGGTTGTAGAGTG
$Ca_V2.1$[EFa] (mouse + human)	m/h.Ca_V2.1[EFa]_Fw	GTCCTCATAGGGTTGCTTGC	m/h.Ca_V2.1[EFa/b]_Rv	GGCAGGTCCATCCGCAG
$Ca_V2.1$[EFb] (mouse + human)	m/h.Ca_V2.1[EFb]_Fw	CCTGGGTCTGGGGAAGAAGT	m/h.Ca_V2.1[EFa/b]_Rv	GGCAGGTCCATCCGCAG
ß-Actin	ß-Actin_Fw	TTGCTGACAGGATGCAGAAG	ß-Actin_Rv	AGTCCGCCTAGAAGCACTTG
GAPDH	GAPDH_Fw	TGTGTCCGTCGTGGATCTGA	GAPDH_Rv	CCTGCTTCACCACCTTCTTGA

Figure S3. RT-qPCR primers. (A) Primer location. **(B)** Primer sequences.

Supplemental Methods

Lentiviral vector construction

The pLL-Syn-h.AU1-Ca_V2.1[EFa] and pLL-Syn-h.AU1-Ca_V2.1[EFb] lentiviral constructs were made by inserting h.Ca_V2.1[EFa/b] (Thalhammer et al., 2017) into the pLL-Syn vector (Jaudon et al., 2022) using the NheI and XbaI restriction sites.

Primary cortical cultures

Cortical neuronal cultures were prepared from P0 C57BL/6J pups as previously described (Jaudon et al., 2022; Thalhammer et al., 2017). Cortices were dissected in ice-cold HBSS, digested with papain (30 U; cat. no. 3126, Worthington) for 40 min at 37°C, washed, and triturated in attachment medium (BME medium supplemented with 10% FBS, 3 mg/mL glucose, 1 mM sodium pyruvate, and 10 mM HEPES-NaOH [pH 7.40]) with a flame-polished glass Pasteur pipette. For RT-qPCR and Western blot experiments, cells were seeded at a concentration of 750,000/well onto 6-well plates coated with 2.5 mg/mL poly-D-lysine (PDL; P7405, Sigma) and 1 mg/mL laminin (L2020, Sigma); for superresolution microscopy experiments, cells were seeded at 75,000/well onto 1.2 cm diameter glass coverslips coated with PDL/laminin as above. After 4 hrs, the attachment medium was replaced with maintenance medium (neurobasal medium supplemented with 2.6% B27, 6 mg/mL glucose, 2 mM GlutaMax, 90 U/mL penicillin, and 0.09 mg/mL streptomycin). To prevent glia overgrowth, cytosine β-D-arabinofuranoside (AraC; 0.5 mM) was added at 5 DIV.

Lentivirus production and infection

Lentiviruses were produced at the Viral Core Facility of the Charité - Universitätsmedizin Berlin (https://vcf.charite.de). Titers were 2.96 x 10^9 for Ca_V2.1[EFa] and 2.2 x 10^9 for Ca_V2.1[EFb]. Neuronal cultures were infected at 7 DIV with the lowest infectious dose capable of transducing >95% of neurons (dilution range: 1:300 to 1:700) and used for experiments after > 10 days.

RNA extraction and RT-qPCR

Total RNA was extracted with TRIzol™ Reagent (Cat. No. 15596026, Thermo Fisher Scientific) at 18 DIV, as previously described (Jaudon et al., 2022; Thalhammer et al., 2018). cDNA was prepared by reverse transcription of 1 µg of RNA using the QuantiTect Reverse Transcription Kit (Cat. No. 205311, Qiagen). RT-qPCR was performed in triplicate with 10 ng of template cDNA using iQTM SYBR® Green Supermix (Cat. No. 1708886, Biorad) on a CFX96 Real-Time PCR Detection System (Biorad) with the following universal conditions: 5 min at 95˚C, 45 cycles of denaturation at 95˚C for 15 s and annealing/extension at 60˚C for 45 s. The relative quantification of gene expression was determined using the ΔΔCt method. Data were

normalized to glyceraldehyde-3-phosphate dehydrogenase (Gapdh) and β-actin (Actb) by the multiple internal control gene method with GeNorm algorithm (Vandesompele et al., 2002). Absolute quantification was performed using the standard curve method. Calibration curves were constructed using five 10-fold serial dilutions of recombinant plasmids harboring target sequence. Sequences and location of all the primers used are listed in Figure S3.

Western blotting

Membrane protein-enriched fractions were prepared from cortical neurons at 18 DIV. Briefly, cells were washed once in ice-cold PBS and scraped in 100 µl buffer A (25 mM Tris-HCl [pH 7.4], 150 mM NaCl, 2 mM KCl, 2.5 mM EDTA) supplemented with protease and phosphatase inhibitors (complete EDTA-free protease inhibitors [cat. no. 1187358001, Roche]; serine/threonine and tyrosine phosphatase inhibitors [cat. nos. P0044 and P5726, Sigma]). After removal of the cell debris at 1,000 g, 4°C, for 10 min, the supernatant was centrifuged at 15,000 g, 4°C, for 15 min. The resulting pellet was dissolved in 100 µl RIPA buffer (50 mM Tris [pH 8.0], 150 mM NaCl, 1% NP-40, 0.5% sodium deoxycholate, 0.1% SDS) and centrifuged at 15,000 g, 4°C, for 15 min. The resulting supernatant was used for Western blot analysis. Protein concentration was quantified with the BCA Protein Assay kit (cat. no. 23227, Thermo Fisher Scientific). Proteins were separated by SDS-PAGE using 7.5% acrylamide gels and transferred on polyvinylidene fluoride (PVDF) membranes. After incubation with primary rabbit anti-$Ca_V2.1$ (1:500; cat. no. 152203, Synaptic Systems) or rabbit anti-β-tubulin III (1:1,000; cat. no. T2200, Sigma) antibodies, membranes were incubated with secondary HRP-conjugated goat anti-rabbit antibody (1: 5,000; cat. no. 31460, Thermo Fisher Scientific) and immunocomplexes were detected with the chemiluminescent substrate (cat. no. RPN2106, ECL Prime Western Blotting System, GE Healthcare). Chemiluminescent signals were acquired using a ChemiDoc imaging system (Biorad).

Immunostaining, SIM microscopy and Image analysis

Cultures were fixed at 20 DIV with Glyoxal (Richter et al., 2018) and blocked at RT in blocking buffer (4% Goat serum, 0,1% BSA in PBS) for 1 hr before o/n incubation with antibodies against $Ca_V2.1$ (rabbit; 1:1000; Synaptic Systems, #152203), vGlut1 (guinea pig; 1:1000; Synaptic Systems; #135304), Bassoon (mouse; 1:250; Synaptic Systems; #141011) and/or Munc13-1 (guinea pig; 1:500; Synaptic Systems; #126115). Coverslips were washed in blocking buffer (8 x 5 min), incubated for 1 hr at RT with goat secondary antibodies (1:800; ThermoFisher; Alexa 405 anti-mouse, #A31553; Alexa 488 anti-rabbit, #A11034; Alexa 647 anti-guinea pig, #A21450), washed in PBS and mounted using Prolong Gold (ThermoFisher).

Images were acquired on a Zeiss Elyra 7 structured illumination microscope (SIM) using a 63x objective with NA 1.46; 0.210 µm step size in the Z direction and 13 phases for SIM acquisition, then reconstructed using the SIM default parameters in Zen Black 3.0. Using FIJI (https://imagej.net/software/fiji/), size and colocalization of puncta were automatically determined after maximum projection of the Z-stack and image thresholding with the Otsu and watershed algorithms.

References

Jaudon, F., Thalhammer, A., Zentilin, L., and Cingolani, L.A. (2022). CRISPR-mediated activation of autism gene Itgb3 restores cortical network excitability via mGluR5 signaling. Mol Ther Nucleic Acids *29*, 462-480.

Richter, K.N., Revelo, N.H., Seitz, K.J., Helm, M.S., Sarkar, D., Saleeb, R.S., D'Este, E., Eberle, J., Wagner, E., Vogl, C., Lazaro, D.F., Richter, F., Coy-Vergara, J., Coceano, G., Boyden, E.S., Duncan, R.R., Hell, S.W., Lauterbach, M.A., Lehnart, S.E., Moser, T., Outeiro, T.F., Rehling, P., Schwappach, B., Testa, I., Zapiec, B., and Rizzoli, S.O. (2018). Glyoxal as an alternative fixative to formaldehyde in immunostaining and super-resolution microscopy. EMBO J *37*, 139-159.

Thalhammer, A., Contestabile, A., Ermolyuk, Y.S., Ng, T., Volynski, K.E., Soong, T.W., Goda, Y., and Cingolani, L.A. (2017). Alternative Splicing of P/Q-Type Ca2+ Channels Shapes Presynaptic Plasticity. Cell Rep *20*, 333-343.

Thalhammer, A., Jaudon, F., and Cingolani, L.A. (2018). Combining Optogenetics with Artificial microRNAs to Characterize the Effects of Gene Knockdown on Presynaptic Function within Intact Neuronal Circuits. J Vis Exp.

Vandesompele, J., De Preter, K., Pattyn, F., Poppe, B., Van Roy, N., De Paepe, A., and Speleman, F. (2002). Accurate normalization of real-time quantitative RT-PCR data by geometric averaging of multiple internal control genes. Genome Biol *3*, RESEARCH0034.